

# Silver-Free Gold Nanocages with Near-Infrared Extinctions

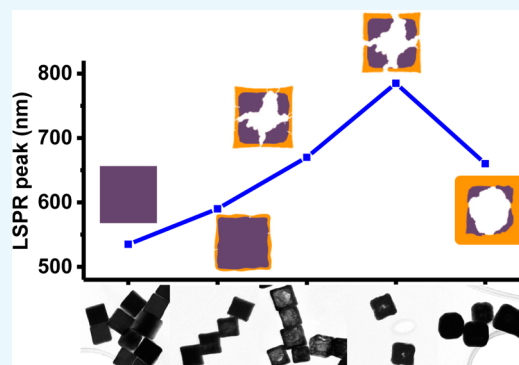
Amin Shakiba,<sup>†,‡</sup> Shreya Shah,<sup>†,‡</sup> Andrew C. Jamison,<sup>†,‡</sup> Irene Rusakova,<sup>‡</sup> Tai-Chou Lee,<sup>§</sup> and T. Randall Lee<sup>\*,†,‡</sup>

<sup>†</sup>Department of Chemistry and <sup>‡</sup>The Texas Center for Superconductivity, University of Houston, 4800 Calhoun Road, Houston, Texas 77204, United States

<sup>§</sup>Department of Chemical and Materials Engineering, National Central University, 300 Jhongda Road, Jhongli City 32001, Taiwan

## Supporting Information

**ABSTRACT:** This article reports the preparation of silver-free Au nanocages from cubic palladium templates. Pd nanocubes were subjected to galvanic replacement with Au<sup>3+</sup> to produce Pd@Au nanocages having tunable dimensions (i.e., edge length, gold layer thickness, and hollow pore size), which allowed selectable positioning of the optical extinction maxima from the visible to the near infrared. These new nanocages circumvent the problems associated with previous Ag-derived gold alloy nanocages, which suffer from the toxicity of residual silver and the possible fragmentation of such alloyed nanostructures, thereby limiting their potential applications. In contrast, the present materials represent stable, nontoxic, tunable, and hollow plasmonic nanostructures.



## INTRODUCTION

Among the various nanoparticle architectures being pursued for optical, catalytic, energy collection/conversion, and theranostic applications,<sup>1–4</sup> hollow nanocages and nanoframes have drawn intense interest due to the potential utilization of their inner void space.<sup>5–8</sup> This feature enables the rapid diffusion of chemicals to and from confined reactive sites, leading to an increase in catalytic activity<sup>9,10</sup> and the potential for payload storage and delivery.<sup>6,7,11</sup> These nanostructures also exhibit an enhanced interaction with light and the surrounding media due to their greater exposed surface area as compared to that of solid nanoparticles. Furthermore, a high surface-to-volume ratio represents a more efficient applications design given the high cost of noble metals such as Pt, Pd, and Au. Notably, an additional requirement for nanomedicinal applications is that these nanoparticles should ideally adsorb/scatter light in the near-infrared (NIR)—a region of the light spectrum where human tissue exhibits little or no adsorption.<sup>12</sup>

Typically, hollow nanostructures, such as nanocages, are synthesized using a core metal particle as a sacrificial template, followed by a galvanic reaction with the salt of a second metal that both engages in a redox reaction with the first metal, slowly oxidizing the metal of the core particle, and deposits on the template surface upon reduction.<sup>13</sup> Silver, which enjoys a low reduction potential (AgCl/Ag<sup>0</sup>, 0.22 V vs SHE),<sup>14</sup> has been the most common sacrificial metal reported for galvanic replacement to produce various types of hollow nanostructures.<sup>1,5,13,15</sup> Starting with an Ag template, NIR-active Au nanocages, nanoframes, and hollow nanoshells can be formed concomitantly with a slight increase in diameter over the template. Xia and co-workers have conducted extensive research in the

development of such silver-templated hollow nanostructures for use in biomedical applications.<sup>7,11</sup> Separate studies have argued that hollow nanostructures, which contain residual silver from the initial template, can undergo fragmentation upon irradiation in vivo.<sup>16</sup> Additionally, the known toxicity of silver limits the clinical usage of silver-templated nanostructures.<sup>17–19</sup> In contrast, Pd-based nanostructures have shown good biocompatibility.<sup>20–24</sup>

A variety of other noble metal combinations in the form of “nanocages” have also been reported, in which the resulting nanostructure is a hollow double-shelled nanocube (NC), an architecture that has reduced interior access as compared to that in a nanoframe.<sup>25</sup> For drug-release applications, easy access to the hollow core is necessary for efficient drug loading, but this requirement must be balanced by the need to control delivery of the drug. Recently, Park and co-workers proposed a new approach to growing a gold shell on a platinum framework, producing a variety of nanorings.<sup>26</sup> These researchers also synthesized Au nanoframes over multiple steps that exhibited NIR extinctions.<sup>27</sup> Such efforts provide insight into how judicious choices in the approach to synthesizing nanostructures can significantly impact the size, shape, and composition of the product. These reports also reveal the varying terminology used to describe the nanostructures involved. In this article, we have chosen to use the term “nanocage” rather than “nanoframe” for our targeted hollow nanostructures

Received: July 19, 2016

Accepted: September 5, 2016

Published: September 21, 2016

because they have limited access to the interior void space afforded by their facial openings.

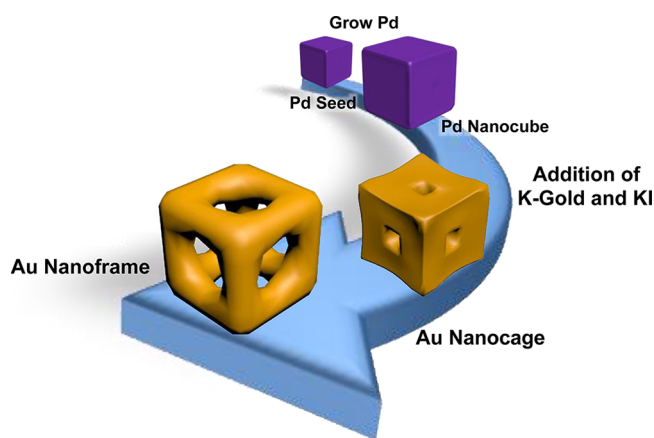
To address the shortcomings noted above, we sought to prepare NIR-active silver-free gold nanocages by starting with palladium NCs as nontoxic, inert templates.<sup>20–24</sup> Palladium also exhibits a significantly higher bulk melting point than that of Ag, which leads to its enhanced photothermal stability.<sup>23</sup> Given these collective considerations, various types of Pd nanoparticles have shown promise in photothermal therapies.<sup>21,22</sup> Several strategies have been developed for the synthesis of Pd NCs in a broad range of sizes to enable the tuning of the localized surface plasmon resonance (LSPR) of the resulting palladium nanoparticles.<sup>28–30</sup> Such NC structures typically produce an extinction maximum at a longer wavelength due to their sharp corners and edges. But the higher scattering cross-section ( $Q_{\text{sca}}$ ) compared to that for absorption ( $Q_{\text{abs}}$ ) for the larger sizes of Pd nanoparticles<sup>29</sup> and strong intrinsic plasmon damping<sup>31</sup> limits the efficiency of Pd NCs for use as light-triggered nanomaterials. On the other hand, gold exhibits a strong absorption cross-section and is known for its biocompatibility and stability in biological media. Recently, studies have explored the use of Pd NCs as templates for the synthesis of hollow nanostructures using Pt and Rh salts for the galvanic reaction.<sup>32–34</sup> However, neither of these combinations of metals would afford particles having optical extinctions in the NIR. Therefore, we sought to take advantage of the outstanding properties of Au coupled with the thermal stability and nontoxicity of Pd templates to design nanocages (Pd@Au nanocages) for their ultimate use in the photothermally initiated release of small molecules for biomedical applications.

At first glance, the galvanic reaction we propose appears to be favored because the standard reduction potential of  $\text{Pd}^{2+}/\text{Pd}^0$  (0.951 V vs SHE) is slightly lower than the one for  $\text{AuCl}_4^-/\text{Au}^0$  (1.002 V vs SHE), but the reduction of  $\text{Au}^{3+}$  to  $\text{Au}^0$  is a two-step process:  $\text{AuCl}_4^-/\text{AuCl}_2^-$  (0.926 V vs SHE) and  $\text{AuCl}_2^-/\text{Au}^0$  (1.154 V vs SHE).<sup>35</sup> As a consequence, we concluded that a direct galvanic replacement between Pd NCs and the  $\text{AuCl}_4^-$  salt would be unfavored (even though the authors of a 2007 study on Au–Pd bimetallic systems concluded that a redox transmetallation reaction does occur between  $\text{Au}^{3+}$  and  $\text{Pd}^0$ ,<sup>36</sup> but the inclusion of hydrazine in their reaction conditions brings their assertions into question). Our concerns regarding the reduction potentials disfavoring a reaction were validated by the results obtained from energy-dispersive X-ray (EDX) spectroscopy for the reaction of Pd NCs with a large amount of Au(III) salt solution: EDX showed no significant levels of Au in the nanoparticles after reaction for 2 h at 80 °C (see Table S1). On the other hand, although Au(I) is thermodynamically capable of undergoing galvanic replacement, disproportionation of Au(I) to Au(0) and Au(III) limits the use of  $\text{AuCl}_2^-$  as a gold precursor for galvanic replacement.<sup>14</sup> One frequently used method to enable this redox chemistry is to add excess halide ions (i.e., chloride and bromide), but the use of these halides requires high temperatures and long reaction times (5–6 h),<sup>36,37</sup> which is ineffective for controlling the morphology during the synthesis of hollow nanostructures.

To overcome these problems, we sought a strategy to lower the reduction potential of  $\text{Pd}^0$  and increase the reduction potential of Au(III) to facilitate the plating process. We achieved the former by adding potassium iodide (KI), leading to the formation of  $\text{PdI}_4^{2-}$ , which enjoys a significantly diminished reduction potential ( $\text{PdI}_4^{2-}/\text{Pd}^0$ , 0.228 V vs

SHE).<sup>38</sup> With regard to Au(III), we employed “K-gold” solution as a gold precursor, which corresponds to a stabilized Au(III) precursor formed under basic conditions (see Methods for details); the use of K-gold increases the reduction potential of Au(III) by ~0.45 V compared to that of Au(III) from  $\text{HAuCl}_4$ .<sup>35</sup> This approach, illustrated in Scheme 1, offers a unique and effective strategy for the galvanic reaction of Au ions with Pd templates.

**Scheme 1. Synthetic Strategy for Producing Au Nanocages and Au Nanoframes<sup>a</sup>**



<sup>a</sup>Both K-gold and KI are necessary for the galvanic reaction.

## METHODS

**Materials.** Potassium tetrachloropalladate ( $\text{K}_2\text{PdCl}_4$ , 99%; STREM Chemicals), hydrogen tetrachloroaurate(III) hydrate ( $\text{HAuCl}_4$ , 99.99%; STREM Chemicals), L-ascorbic acid (AA, 99%; Sigma-Aldrich), cetyltrimethyl ammonium bromide (CTAB, 98%; Amresco), hydrochloric acid (HCl, 37%; Macron Fine Chemicals), nitric acid ( $\text{HNO}_3$ , 68–70%; Macron Fine Chemicals), and anhydrous potassium carbonate (J.T. Baker) were purchased from the indicated suppliers. Water was purified to a resistivity of 18.2  $\text{M}\Omega\cdot\text{cm}$  (Academic Milli-Q Water System; Millipore Corp.). All glassware was cleaned with aqua regia solution (HCl/ $\text{HNO}_3$ ; 3:1), thoroughly rinsed with Millipore water, and dried prior to use.

**Pd NC Seed Synthesis.** The Pd NC seed solution was synthesized by reduction of  $\text{K}_2\text{PdCl}_4$  by AA. A total of 24.0 mL of CTAB solution (50 mM) was prepared by dissolving 437 mg of CTAB in 24.0 mL of Millipore water under vigorous stirring in a 50 mL round bottom flask suspended in an oil bath, followed by the initiation of refluxing at 100 °C. To this solution, while still refluxing, 10.0 mL of  $\text{K}_2\text{PdCl}_4$  (5 mM; aqueous solution) and 1.00 mL of AA (300 mM; aqueous solution) were added and kept under constant stirring for 5 h. The resulting suspension was cooled to room temperature and centrifuged at 8000 rpm for 20 min, followed by decantation of the supernatant and redispersion in 10.0 mL of Millipore water. The centrifugation process was repeated two times. The resulting Pd NC seed suspension had a concentration of  $1.31 \times 10^{11}$  particles/mL.

**Pd NC Synthesis.** A 60.0 mL sample of 50 mM CTAB solution was prepared by adding 1.09 g of CTAB in 60.0 mL of Millipore water with vigorous stirring at 40 °C. Once the CTAB was completely dissolved, 6.00 mL of  $\text{K}_2\text{PdCl}_4$  (5 mM) and 1.20 mL of aqueous HCl (100 mM) were added to the

solution. After waiting for 5 min, 480  $\mu\text{L}$  of Pd NC seeding solution was added. Finally, 600  $\mu\text{L}$  of aqueous AA solution (100 mM) was added. The resulting solution was vigorously stirred, and the temperature was maintained at 40  $^{\circ}\text{C}$  for 4 h in an oil bath. The prepared Pd NCs were washed with Millipore water and centrifuged two times at 6000 rpm for 10 min, followed by decantation of the supernatant and redispersion in 45.0 mL of Millipore water. The resulting NC suspension had a concentration of  $5.87 \times 10^9$  particles/mL, and the synthesized Pd NCs had an average edge length of 85 nm.

To synthesize different sizes of Pd NCs, we followed the same synthetic procedure but with differing amounts of Pd NC seed solution added. A 500  $\mu\text{L}$  aliquot of Pd NC seed solution was used to obtain Pd NCs with an average edge length of 65 nm, whereas 450  $\mu\text{L}$  of Pd NC seed solution was added to obtain Pd NCs with an average edge length of 105 nm.

**Preparation of K-Gold Solution.** A solution containing a reducible gold salt (K-gold solution) was first prepared by dissolving 30.0 mg of anhydrous potassium carbonate in 100 mL of Millipore water. After 5 min of stirring, 2 mL of 1 wt %  $\text{HAuCl}_4$  aqueous solution was added to the potassium carbonate solution, which was then stirred for 2 h to form a colorless solution. The K-gold solution was then aged at 4  $^{\circ}\text{C}$  in darkness for a minimum of 2 days.

**Galvanic Replacement of Pd with K-Gold.** Au nanocages were synthesized by galvanic replacement of Pd with Au. In a standard procedure, 6.00 mL of Pd NC solution, 300  $\mu\text{L}$  of KI (from a 5 mM KI solution), and 50 mg of CTAB were added to a 40 mL vial. This mixture was heated to 50  $^{\circ}\text{C}$  in an oil bath with constant stirring at 400 rpm and kept at that temperature for 30 min. A 4.00 mL aliquot of K-gold solution was then added to the flask, the temperature was raised to 80  $^{\circ}\text{C}$ , and this temperature was maintained for 1.5 h. The resulting solution was then centrifuged at 5000 rpm, the supernatant was decanted, and the particles were redispersed in Millipore water. This procedure was repeated two times with the as-synthesized Pd@Au nanocages being redispersed in 6.00 mL of Millipore water.

The amount of added KI and K-gold influences the course of the galvanic replacement reaction. Four representative samples of the Pd@Au nanocages (4 stages) were synthesized to illustrate the process of nanocage growth during the galvanic reaction. Also, an Au nanoframe was prepared by expanding the size of the facial openings of the nanocage as compared to that of the third-stage nanocage (Pd@Au 3). Separately, a Pd@Au nanoparticle having a spherical shape was synthesized using relatively large amounts of KI and K-gold. The reactants needed to prepare the nanoparticles representing the four stages of nanocage growth as well as the nanoframes and nanospheres are summarized in Table S2.

**Characterization.** The morphology of the nanoparticles was evaluated using a FEI-235 scanning electron microscope (SEM), operating at an accelerating voltage of 15 kV. To obtain high-resolution (HR) SEM images, all samples were deposited on silicon wafers. Transmission electron microscopes (TEMs); FEI G2, JEOL 2000 FX, and JEM 2010 equipped with energy-dispersive spectrometers; were operated at either 100 or 200 kV. Conventional and HR TEM imaging, selected area electron diffraction (SAED), and EDX spectroscopy, including elemental mapping methods, were used for analysis of the nanoparticles. All TEM samples were deposited on 300 mesh holey carbon-coated copper grids and dried before analysis. UV–visible (UV–vis) extinction spectra were obtained using a

Cary 50 Scan UV–vis spectrometer over the wavelength range of 200–1100 nm. A Siemens D-5000 powder X-ray diffractometer equipped with a monochromatic  $\text{Cu K}\alpha$  ( $\lambda = 1.540562 \text{ \AA}$ ) radiation source was used to analyze the samples over the  $2\theta$  range 5–90 $^{\circ}$  in steps of 0.02 $^{\circ}$ . The concentrations of the suspensions at each step of the synthesis procedure were measured with a Malvern Instruments NanoSight NS300 nanoparticle tracking system.

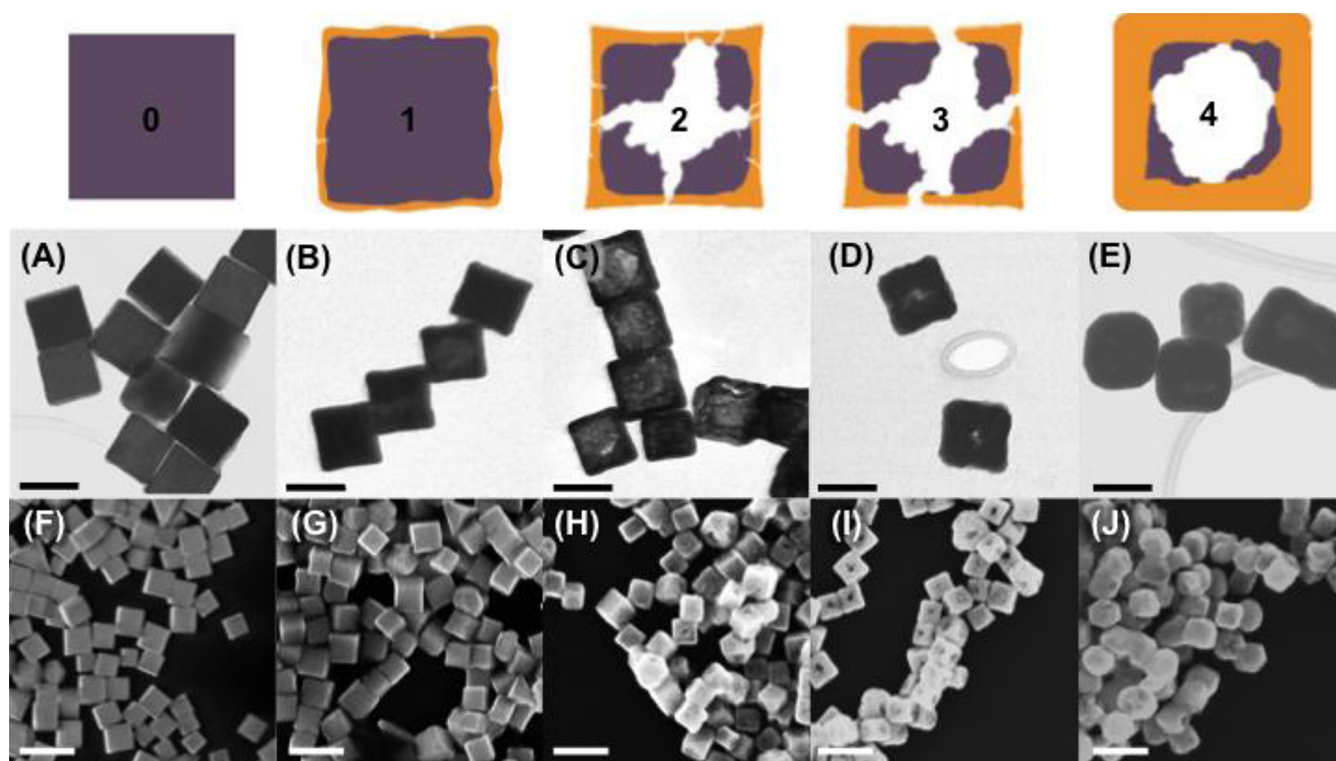
## RESULTS AND DISCUSSION

We synthesized the template Pd NCs using seed-mediated growth (see Figure S1 for TEM images of the Pd “seeds”). The procedure successfully produced Pd NCs with sharp edges and corners. Figures 1A,F show the TEM and SEM images, respectively, for the 105 nm Pd NCs used for the preparation of the nanocages; for the sake of simplicity, we provide a cartoon illustration above each set of images (i.e., Illustration 0 corresponds to the Pd NCs in Figures 1A,F). The powder X-ray diffraction (XRD) pattern in Figure S2 shows an intense peak for the (200) lattice of face-centered cubic (fcc,  $Fm\bar{3}m$  (225)) crystalline Pd, which indicates most of the Pd NCs preferentially oriented with {100} facets parallel to the deposition surface.<sup>29</sup> This pattern is consistent with the formation of the sharp edges for our Pd NCs, which can also be observed in the TEM images in Figure S1.

We then subjected the Pd NCs to galvanic replacement with Au. To determine the optimum reaction conditions, we undertook a systematic study of the galvanic reaction by varying the amounts of KI and K-gold solution to investigate the morphological changes during the galvanic replacement process.<sup>13</sup> After analyzing the results from over 100 reactions, we noted several reaction products in which changes in the amount of added KI and K-gold solution were associated with a reaction pathway that included four stages of nanocage development. Using the knowledge gained from these studies, we fixed the reaction time at 1.5 h for all syntheses of the nanocages/nanoframes, which was sufficient for complete reaction. Additionally, K-gold was used as our limiting reagent, an approach similar to the strategies used in prior reports.<sup>5,14</sup> Furthermore, we added only a moderate excess of KI for each reaction. The reactants used for each of the synthesized nanostructures are summarized in Table S2, and the corresponding results are displayed in Figure 1. The illustrations on the top row show the growth of the nanocages as a function of increasing amount of added K-gold/KI solution. The illustrations are consistent with the EDX mapping analyses for each stage (see Figure S3).

Figures 1B,G show, respectively, the TEM and SEM images of nanocages formed during the first stage of the galvanic replacement reaction (see also Illustration 1). Notably, dilute reactants (i.e., 50  $\mu\text{L}$  of KI and 0.10 mL of K-gold solution) generate a thin layer of Au that forms on the surface of the Pd template as some of the Pd is initially oxidized. This thin layer appears to plate preferentially on the templates starting from the edges; according to our EDX data, this sample has only a small amount of Au relative to Pd (see Table S1). Prior investigators hypothesized that the galvanic reaction proceeds by interdiffusion of core metal atoms to the surface of the nanocages at the early stages of the replacement reaction to form an Au–Pd bimetallic shell.<sup>34,39</sup>

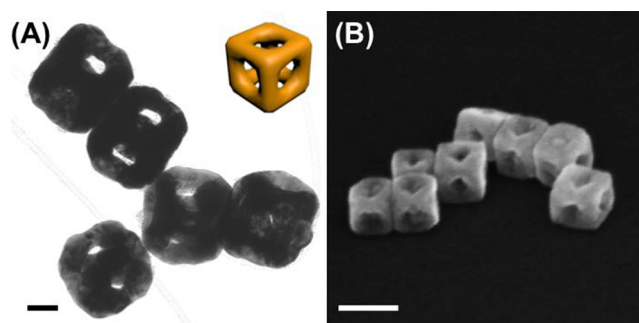
At higher reactant concentrations (i.e., 250  $\mu\text{L}$  of KI and 1.00 mL of K-gold solution), which reflect the second stage of the galvanic reaction, Au continues to replace Pd on the outermost



**Figure 1.** (Top row) Illustration of the morphological changes that occur during the stages of the galvanic replacement reaction between Pd NCs and  $\text{Au}^{3+}$  in solution. (Middle row) TEM images of (A) Pd NCs and (B–E) Pd@Au nanocages at various stages of the reaction accomplished by increasing the amount of KI and K-gold solution. All TEM images are at the same magnification showing 100 nm scale bars. (Bottom row) SEM images of (F) Pd NCs and (G–J) Pd@Au nanocages at the various stages of the reaction. All SEM images are at the same magnification showing 200 nm scale bars.

layer of the nanocages. The diffused Pd atoms in the growing shell oxidize, and pinholes begin to form on the faces of the template structures, as shown in Figures 1C,H (see Illustration 2), allowing ions to diffuse from the core.<sup>14</sup> A previous study showed that iodide ions, when used in conjunction with CTAB, act as capping agents on the various facets of Pd, with the adsorption of these ions leading to the following order of surface energies for the crystallographic planes:  $\{111\} > \{100\} > \{110\}$ .<sup>40</sup> Therefore, the presence of KI influences the morphology of the nanocages over the course of the galvanic reaction. Herein, we take advantage of this reactivity of  $\text{I}^-$ , which plausibly helps activate the Pd atoms in the  $\{111\}$  facets (and perhaps the  $\{100\}$  facets) for oxidation and/or diffusion. Additionally, researchers have suggested that the generated electrons from the cathodic reaction migrate to the surface and the incoming Au atoms are initially kinetically favored to deposit on sharp edges and corners, which have higher surface free energies.<sup>41,42</sup> This phenomenon leads to the formation of a concave-type structure with sharp edges and corners. All of the above contribute to a key feature of our synthesis method: the size of the openings that develop at the center of the faces of the nanocages can be tuned by changing the amount of K-gold precursor solution used. To this end, we used 300  $\mu\text{L}$  of KI and 4.00 mL of K-gold solution to illustrate the products at the third stage of the galvanic reaction (see Figures 1D,I; Illustration 3). Importantly, the formation of nanocages can be redirected to produce nanoframes instead by further increasing the K-gold solution used to 5.00 mL (see Figure 2).

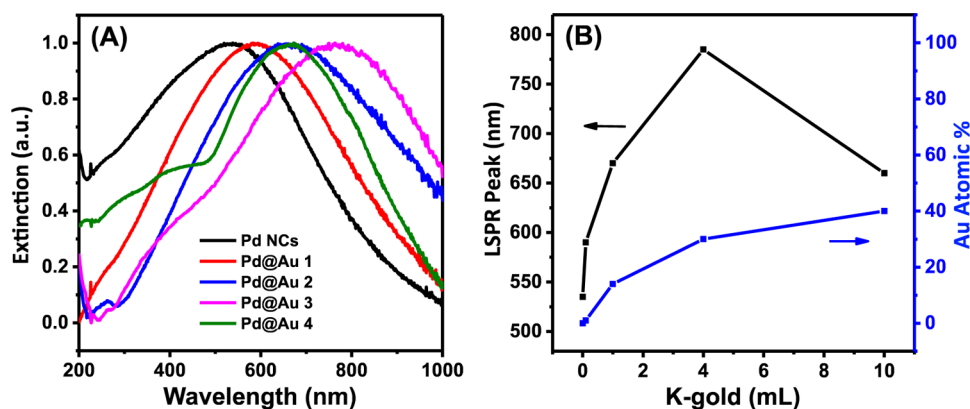
In the final stage of the galvanic reaction, induced by using 500  $\mu\text{L}$  of KI and 10.0 mL of K-gold solution (see Figures 1E,J;



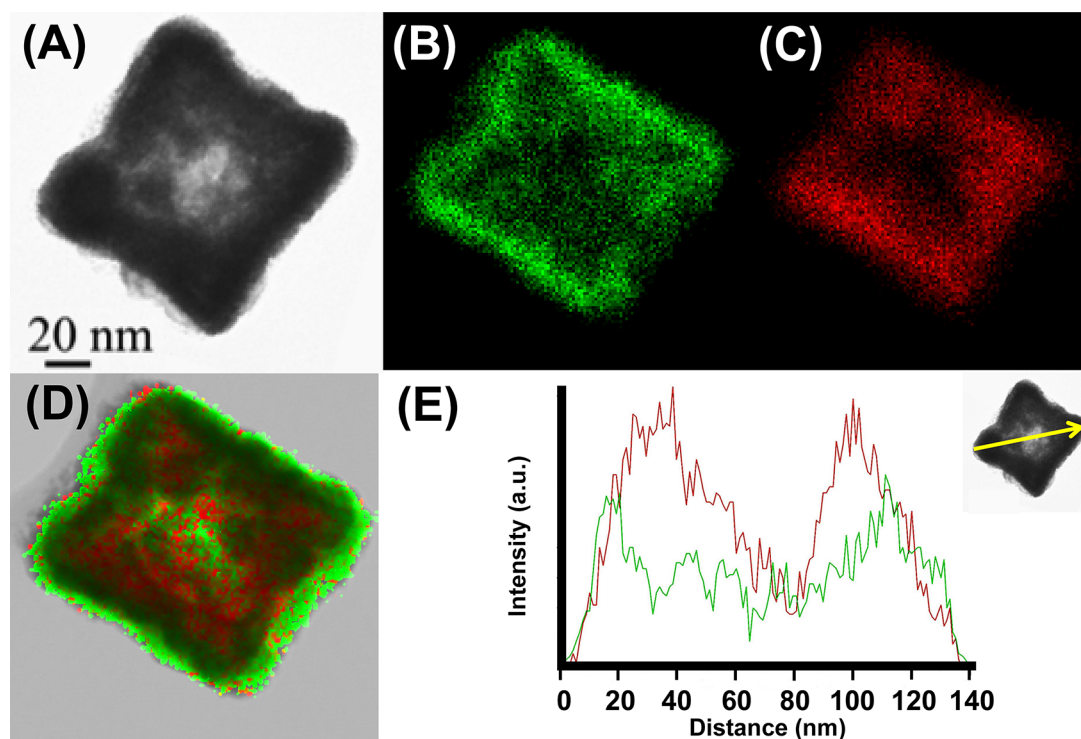
**Figure 2.** (A) TEM image of Pd@Au nanoframes prepared by increasing the amount of KI and K-gold solution during the third stage of the galvanic reaction. The TEM image scale bar is 50 nm. The inset drawing in (A) shows a 3D model of a nanoframe. (B) A tilted SEM image of the same Pd@Au nanoframes. The SEM image scale bar is 200 nm, and the stage was tilted at 45°.

Illustration 4), we observe a total disappearance of the openings in the faces of the nanocages as the particles develop continuous shells. According to the EDX data (Table S1), the amount of Pd in the structure remains substantial, which indicates that closure of the openings can take place earlier than that reported in previous studies with Au–Ag nanocages.<sup>14</sup> This phenomenon can be attributed to the different stoichiometries of the galvanic reactions for Au/Pd as compared to those for Au/Ag.

According to eq 1, three  $\text{Pd}^0$  atoms are oxidized to reduce two atoms of  $\text{Au}^{3+}$ . For the Au–Ag system, three silver atoms



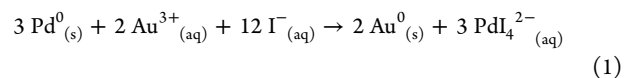
**Figure 3.** (A) Normalized extinction spectra of the products from the galvanic replacement reactions (and including the initial Pd NCs) using varying amounts of KI and K-gold solution. (B) Plot of the LSPR peak positions vs the volume of K-gold solution, as compared to the atomic percentage of Au in these nanostructures after each galvanic reaction, as measured by EDX (see Tables S1 and S2 for additional details).



**Figure 4.** Compositional analysis of the Pd@Au nanocages formed during the third stage of galvanic replacement (3 in Figure 1). (A) TEM image of an individual Pd@Au 3 nanocage; (B–D) the EDX mapping images of (B) Au, (C) Pd, and (D) both Au and Pd; and (E) the EDX line profile along the diagonal direction. The inset image illustrates the mapping along the yellow line (Pd: red and Au: green).

are oxidized by one  $\text{Au}^{3+}$  ion. Therefore, the oxidation of Pd engenders the deposition of a larger volume of Au and, consequently, the gold shell develops with a significant amount of Pd remaining underneath. Importantly, Pd NPs have been shown to be biocompatible in biomedical applications.<sup>22–24</sup> Also, the presence of Pd in the nanocage skeleton is known to increase the stability of nanoparticles at low pH.<sup>43</sup> Further, the metals in Pd-coated Au NCs remain separated upon heating to temperatures greater than 250 °C.<sup>44</sup> Moreover, studies of Pd–Au bimetallic clusters have found the Pd-core/Au-shell structure to be the most stable upon annealing at elevated temperatures.<sup>45</sup> However, one downside is that the presence of Pd decreases the photothermal efficiency of the corresponding nanostructures. Future studies will explore a suitable etching

process to reduce the remaining Pd and enhance the plasmonic efficiency.



To gain further insight into the evolution of the Pd@Au nanocages, we recorded extinction spectra of the nanocages over the four stages of galvanic replacement. The extinction spectra in Figure 3 are normalized, which is a common practice when reporting the spectra of nanoboxes and nanocages.<sup>5</sup> The absolute extinction spectra (i.e., without normalization) are provided in Figure S4. Figure 3A shows that the extinction maxima shift from 540 to 785 nm with increasing K-gold reactant up to a point (i.e., with the formation of Pd@Au 3 as

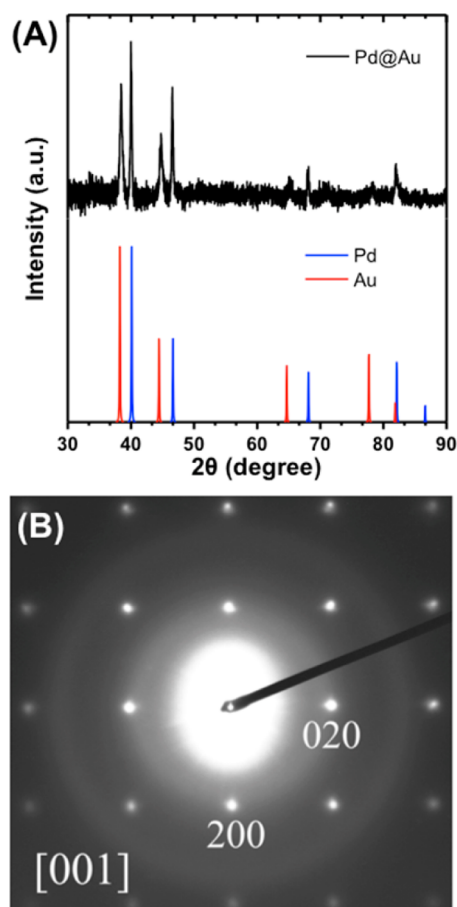


**Figure 5.** (A) Powder XRD pattern of Pd@Au nanocages at the third stage. The reference patterns for Au and Pd are provided (both structures are fcc,  $Fm\bar{3}m$  (225)). (B) SAED pattern recorded from an individual nanocage.

optimized nanocages), whereas the use of 10.0 mL of K-gold produced nanocages with shorter extinction wavelengths (Pd@Au 4). The latter phenomenon arises from the deposition of a thick gold shell, which leads to the disappearance of sharp edges and the concave shape (as shown in Figures 1E,J). The nanoframe structure is produced with a moderate increase in K-gold solution as compared to that in Pd@Au 3, and it has a similar extinction band to that of Pd@Au 3 (see Figure S5). In addition, the presence of residual Pd in Au nanostructures can plausibly give rise to broadening of the extinction band, not only due to the differing positions of the extinction maxima for these two metals,<sup>46</sup> but also due to plasmon damping caused by the incorporation of Pd.<sup>31</sup> Evidence of the latter can be seen by comparing the broad band for the initial Pd@Au to the narrower band for Pd@Au 4 (decreasing ratio of Pd/Au).

To gain a better understanding of the processes involved, we plotted the EDX results in Figure 3B to show that the galvanic reaction continued to take place even as the opening to the interior void closed, giving rise to a thickening of the gold shell. We also provided the composition of the individual Pd@Au nanocages using our EDX data, and the details are provided in Table S1. Despite the encapsulation of the initial template, the Au plating can proceed further with the addition of even greater amounts of K-gold, eventually forming spherical nanoparticles; these particles are shown in Figure S6.

Analysis of our nanocages by EDX indicates the presence of only Au and Pd in these particles (see Figure S7). Furthermore,

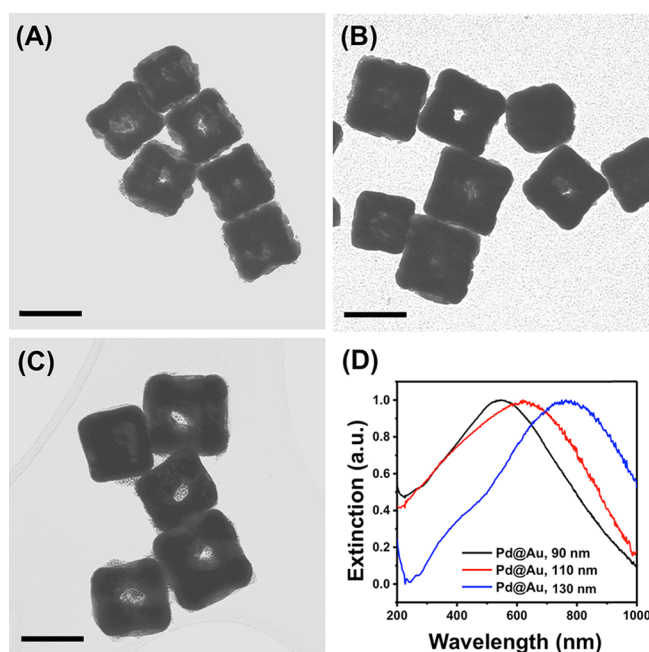


**Figure 6.** TEM images of the Pd@Au nanocages obtained from the (A) 65 nm Pd templates, (B) 85 nm Pd templates, and (C) 105 nm Pd templates. All scale bars are 100 nm. (D) Normalized extinction spectra for the products of the galvanic replacement reactions with the three different edge lengths of Pd NCs.

Figure 4 provides the characterization of the optically optimized Pd@Au 3 nanocages by TEM and EDX. Specifically, Figures 4B–D provide the mapping images, and Figure 5E provides the EDX line profiles recorded from the individual Pd@Au 3 nanocage shown in Figure 4A along the diagonal direction of the face of the cube. These data show that the outer corners and edges exhibited high Au content, whereas the core is essentially hollow, with Pd predominating in the inner shell of the cage structure.

For a more comprehensive investigation of this unique nanostructure, we provide the powder XRD pattern of the Pd@Au 3 nanocages to illustrate the crystal structures of the metal components. Figure 5A depicts a single crystalline fcc cubic structure. The Pd and Au diffraction peaks match those reported for a bimetallic Au–Pd system in which the metals are separated rather than alloyed,<sup>37,44</sup> which strongly suggests that gold and palladium are separated in our nanocages (which is further consistent with the NIR positioning of their extinction maximum). Also, the SAED patterns in Figure 5B recorded from Pd@Au 3 nanocages confirm that they are single crystals, their symmetry is  $Fm\bar{3}m$ , and there is no superlattice ordering of Au or Pd. Also, the SAED pattern shows one set of spots, which confirms that each crystalline component is perfectly overlapped (i.e., during galvanic replacement, the Pd serves as a template to grow the overlying gold layer, and the deposited gold atoms align exactly with the Pd atoms).

Mie theory predicts that a change in the size of nanoparticles causes a shift in their extinction maximum.<sup>47,48</sup> As we sought to produce hollow nanostructures that absorb/scatter light in the NIR, we chose to investigate this aspect of modulating the nanocage design. To this end, we synthesized the Pd@Au nanocages in three different sizes to determine how particle size impacts the optical properties. We started with three sizes of Pd NCs (average edge lengths of 65, 85, and 105 nm) as sacrificial

templates for galvanic replacement, as shown in the TEM images in Figure S1. Figures 6A–C show the TEM images of Pd@Au nanocages after galvanic replacement of the Pd templates. Importantly, the extinction spectra in Figure 6D show that our efforts to use nanocage size to modulate the positioning of the extinction maximum allowed us to tune the extinction band from 570 to 785 nm.

## CONCLUSIONS

In summary, we demonstrated a simple and efficient method for the synthesis of hollow Pd-templated Au nanocages (and nanoframes) that adsorb/scatter light in the NIR. With our approach, we avoided the use of silver templates that are known to be toxic and unstable for biological applications. We investigated the changes in the morphology of the nanocages at different stages of the galvanic replacement reaction. Our results lead us to believe that these Pd@Au nanocages have the potential for application in the fields of drug delivery, optical sensing, and photothermal therapy, owing to their tunable extinction maxima as well as their high surface areas. The new synthesis procedure reported herein can be easily scaled up and will play a key role in the development of hollow nanostructures for biological applications. In-depth evaluations of the stability and toxicity of these unique nanostructures are planned in the near future.

## ASSOCIATED CONTENT

### Supporting Information

The Supporting Information is available free of charge on the ACS Publications website at DOI: 10.1021/acsomega.6b00134.

Additional experimental and characterization detail for the particles prepared for this report (Figures S1–S7, Tables S1–S2) (PDF)

## AUTHOR INFORMATION

### Corresponding Author

\*E-mail: trlee@uh.edu.

### Notes

The authors declare no competing financial interest.

## ACKNOWLEDGMENTS

We thank the Asian Office of Aerospace Research and Development (AFOSR/AOARD FA2386-15-1-4101), the Robert A. Welch Foundation (E-1320), and the Texas Center for Superconductivity for supporting this research. Additionally, the Malvern Nanosight instrument used in this study was acquired using a Defense University Research Instrumentation Program (DURIP) grant (FA9550-15-1-0374) issued by the Air Force Office of Scientific Research.

## REFERENCES

- (1) Vongsavat, V.; Vittur, B. M.; Bryan, W. W.; Kim, J.-H.; Lee, T. R. Ultrasmall Hollow Gold-Silver Nanoshells with Extinctions Strongly Red-Shifted to the Near-Infrared. *ACS Appl. Mater. Interfaces* **2011**, *3*, 3616–3624.
- (2) Khantamat, O.; Li, C.-H.; Yu, F.; Jamison, A. C.; Shih, W.-C.; Cai, C.; Lee, T. R. Gold Nanoshell-Decorated Silicone Surfaces for the Near-Infrared (NIR) Photothermal Destruction of the Pathogenic Bacterium *E. faecalis*. *ACS Appl. Mater. Interfaces* **2015**, *7*, 3981–3993.
- (3) Li, C.-H.; Li, M.-C.; Liu, S.-P.; Jamison, A. C.; Lee, D.; Lee, T. R.; Lee, T.-C. Plasmonically Enhanced Photocatalytic Hydrogen Production from Water: The Critical Role of Tunable Surface Plasmon

Resonance from Gold-Silver Nanoshells. *ACS Appl. Mater. Interfaces* **2016**, *8*, 9152–9161.

- (4) Jain, P. K.; Huang, X.; El-Sayed, I. H.; El-Sayed, M. A. Noble Metals on the Nanoscale: Optical and Photothermal Properties and Some Applications in Imaging, Sensing, Biology, and Medicine. *Acc. Chem. Res.* **2008**, *41*, 1578–1586.

- (5) Lu, X.; Au, L.; McLellan, J.; Li, Z.-Y.; Marquez, M.; Xia, Y. Fabrication of Cubic Nanocages and Nanoframes by Dealloying Au/Ag Alloy Nanoboxes with an Aqueous Etchant Based on Fe(NO<sub>3</sub>)<sub>3</sub> or NH<sub>4</sub>OH. *Nano Lett.* **2007**, *7*, 1764–1769.

- (6) Yavuz, M. S.; Cheng, Y.; Chen, J.; Cobley, C. M.; Zhang, Q.; Rycenga, M.; Xie, J.; Kim, C.; Song, K. H.; Schwartz, A. G.; Wang, L. V.; Xia, Y. Gold Nanocages Covered by Smart Polymers for Controlled Release with Near-Infrared Light. *Nat. Mater.* **2009**, *8*, 935–939.

- (7) Xia, Y.; Li, W.; Cobley, C. M.; Chen, J.; Xia, X.; Zhang, Q.; Yang, M.; Cho, E. C.; Brown, P. K. Gold Nanocages: From Synthesis to Theranostic Applications. *Acc. Chem. Res.* **2011**, *44*, 914–924.

- (8) Mahmoud, M. A.; El-Sayed, M. A. Gold Nanoframes: Very High Surface Plasmon Fields and Excellent Near-Infrared Sensors. *J. Am. Chem. Soc.* **2010**, *132*, 12704–12710.

- (9) Mahmoud, M. A.; Saira, F.; El-Sayed, M. A. Experimental Evidence For The Nanocage Effect In Catalysis With Hollow Nanoparticles. *Nano Lett.* **2010**, *10*, 3764–3769.

- (10) Mahmoud, M. A.; Narayanan, R.; El-Sayed, M. A. Enhancing Colloidal Metallic Nanocatalysis: Sharp Edges and Corners for Solid Nanoparticles and Cage Effect for Hollow Ones. *Acc. Chem. Res.* **2013**, *46*, 1795–1805.

- (11) Cobley, C. M.; Chen, J.; Cho, E. C.; Wang, L. V.; Xia, Y. Gold Nanostructures: A Class of Multifunctional Materials for Biomedical Applications. *Chem. Soc. Rev.* **2011**, *40*, 44–56.

- (12) Hirsch, L. R.; Stafford, R. J.; Bankson, J. A.; Sershen, S. R.; Rivera, B.; Price, R. E.; Hazle, J. D.; Halas, N. J.; West, J. L. Nanoshell-Mediated Near-Infrared Thermal Therapy of Tumors Under Magnetic Resonance Guidance. *Proc. Natl. Acad. Sci. U.S.A.* **2003**, *100*, 13549–13554.

- (13) Jones, M. R.; Osberg, K. D.; MacFarlane, R. J.; Langille, M. R.; Mirkin, C. A. Templated Techniques for the Synthesis and Assembly of Plasmonic Nanostructures. *Chem. Rev.* **2011**, *111*, 3736–3827.

- (14) Au, L.; Lu, X.; Xia, Y. A Comparative Study of Galvanic Replacement Reactions Involving Ag Nanocubes and AuCl<sub>2</sub><sup>-</sup> or AuCl<sub>4</sub><sup>-</sup>. *Adv. Mater.* **2008**, *20*, 2517–2522.

- (15) Li, C.-H.; Jamison, A. C.; Rittikulstitchai, S.; Lee, T.-C.; Lee, T. R. In Situ Growth of Hollow Gold–Silver Nanoshells within Porous Silica Offers Tunable Plasmonic Extinctions and Enhanced Colloidal Stability. *ACS Appl. Mater. Interfaces* **2014**, *6*, 19943–19950.

- (16) Goodman, A. M.; Cao, Y.; Urban, C.; Neumann, O.; Ayala-Orozco, C.; Knight, M. W.; Joshi, A.; Nordlander, P.; Halas, N. J. The Surprising in Vivo Instability of Near-IR-Absorbing Hollow Au–Ag Nanoshells. *ACS Nano* **2014**, *8*, 3222–3231.

- (17) Kittler, S.; Greulich, C.; Diendorf, J.; Köller, M.; Epple, M. Toxicity of Silver Nanoparticles Increases during Storage Because of Slow Dissolution under Release of Silver Ions. *Chem. Mater.* **2010**, *22*, 4548–4554.

- (18) Cheng, X.; Zhang, W.; Ji, Y.; Meng, J.; Guo, H.; Liu, J.; Wu, X.; Xu, H. Revealing Silver Cytotoxicity Using Au Nanorods/Ag Shell Nanostructures: Disrupting Cell Membrane and Causing Apoptosis Through Oxidative Damage. *RSC Adv.* **2013**, *3*, 2296–2305.

- (19) Xiu, Z.-m.; Zhang, Q.-b.; Puppala, H. L.; Colvin, V. L.; Alvarez, P. J. J. Negligible Particle-Specific Antibacterial Activity of Silver Nanoparticles. *Nano Lett.* **2012**, *12*, 4271–4275.

- (20) Wang, J.; Cheng, B.; Li, J.; Zhang, Z.; Hong, W.; Chen, X.; Chen, P. R. Chemical Remodeling of Cell-Surface Sialic Acids through a Palladium-Triggered Bioorthogonal Elimination Reaction. *Angew. Chem., Int. Ed.* **2015**, *54*, 5364–5368.

- (21) Huang, X.; Tang, S.; Yang, J.; Tan, Y.; Zheng, N. Etching Growth under Surface Confinement: An Effective Strategy To Prepare Mesocrystalline Pd Nanocorolla. *J. Am. Chem. Soc.* **2011**, *133*, 15946–15949.

- (22) Tang, S.; Chen, M.; Zheng, N. Sub-10-nm Pd Nanosheets with Renal Clearance for Efficient Near-Infrared Photothermal Cancer Therapy. *Small* **2014**, *10*, 3139–3144.
- (23) Huang, X.; Tang, S.; Mu, X.; Dai, Y.; Chen, G.; Zhou, Z.; Ruan, F.; Yang, Z.; Zheng, N. Freestanding Palladium Nanosheets with Plasmonic and Catalytic Properties. *Nat. Nanotechnol.* **2011**, *6*, 28–32.
- (24) Nie, L.; Chen, M.; Sun, X.; Rong, P.; Zheng, N.; Chen, X. Palladium Nanosheets as Highly Stable and Effective Contrast Agents for In Vivo Photoacoustic Molecular Imaging. *Nanoscale* **2014**, *6*, 1271–1276.
- (25) Mahmoud, M. A.; El-Sayed, M. A. Metallic Double Shell Hollow Nanocages: The Challenges of Their Synthetic Techniques. *Langmuir* **2012**, *28*, 4051–4059.
- (26) Jang, H.-J.; Ham, S.; Acapulco, J. A. I.; Song, Y.; Hong, S.; Shuford, K. L.; Park, S. Fabrication of 2D Au Nanorings with Pt Framework. *J. Am. Chem. Soc.* **2014**, *136*, 17674–17680.
- (27) Ham, S.; Jang, H.-J.; Song, Y.; Shuford, K. L.; Park, S. Octahedral and Cubic Gold Nanoframes with Platinum Framework. *Angew. Chem., Int. Ed.* **2015**, *54*, 9025–9028.
- (28) Xiong, Y.; Chen, J.; Wiley, B.; Xia, Y.; Yin, Y.; Li, Z.-Y. Size-Dependence of Surface Plasmon Resonance and Oxidation for Pd Nanocubes Synthesized via a Seed Etching Process. *Nano Lett.* **2005**, *5*, 1237–1242.
- (29) Niu, W.; Li, Z.-Y.; Shi, L.; Liu, X.; Li, H.; Han, S.; Chen, J.; Xu, G. Seed-Mediated Growth of Nearly Monodisperse Palladium Nanocubes with Controllable Sizes. *Cryst. Growth Des.* **2008**, *8*, 4440–4444.
- (30) Niu, W.; Zhang, W.; Firdoz, S.; Lu, X. Controlled Synthesis of Palladium Concave Nanocubes with Sub-10-Nanometer Edges and Corners for Tunable Plasmonic Property. *Chem. Mater.* **2014**, *26*, 2180–2186.
- (31) Jing, H.; Wang, H. Structural Evolution of Ag–Pd Bimetallic Nanoparticles through Controlled Galvanic Replacement: Effects of Mild Reducing Agents. *Chem. Mater.* **2015**, *27*, 2172–2180.
- (32) Zhang, H.; Jin, M.; Wang, J.; Li, W.; Camargo, P. H. C.; Kim, M. J.; Yang, D.; Xie, Z.; Xia, Y. Synthesis of Pd–Pt Bimetallic Nanocrystals with a Concave Structure through a Bromide-Induced Galvanic Replacement Reaction. *J. Am. Chem. Soc.* **2011**, *133*, 6078–6089.
- (33) Xie, S.; Lu, N.; Xie, Z.; Wang, J.; Kim, M. J.; Xia, Y. Synthesis of Pd–Rh Core–Frame Concave Nanocubes and Their Conversion to Rh Cubic Nanoframes by Selective Etching of the Pd Cores. *Angew. Chem., Int. Ed.* **2012**, *51*, 10266–10270.
- (34) Zhang, L.; Roling, L. T.; Wang, X.; Vara, M.; Chi, M.; Liu, J.; Choi, S.-I.; Park, J.; Herron, J. A.; Xie, Z.; Mavrikakis, M.; Xia, Y. Platinum-Based Nanocages with Subnanometer-Thick Walls and Well-Defined, Controllable Facets. *Science* **2015**, *349*, 412–416.
- (35) Brinson, B. E.; Lassiter, J. B.; Levin, C. S.; Bardhan, R.; Mirin, N.; Halas, N. J. Nanoshells Made Easy: Improving Au Layer Growth on Nanoparticle Surfaces. *Langmuir* **2008**, *24*, 14166–14171.
- (36) Chen, C.-H.; Sarma, L. S.; Chen, J.-M.; Shih, S.-C.; Wang, G.-R.; Liu, D.-G.; Tang, M.-T.; Lee, J.-F.; Hwang, B.-J. Architecture of Pd–Au Bimetallic Nanoparticles in Sodium Bis(2-ethylhexyl)sulfosuccinate Reverse Micelles As Investigated by X-ray Absorption Spectroscopy. *ACS Nano* **2007**, *1*, 114–125.
- (37) Harpeness, R.; Gedanken, A. Microwave Synthesis of Core–Shell Gold/Palladium Bimetallic Nanoparticles. *Langmuir* **2004**, *20*, 3431–3434.
- (38) Liu, S.-Y.; Shen, Y.-T.; Chiu, C.-Y.; Rej, S.; Lin, P.-H.; Tsao, Y.-C.; Huang, M. H. Direct Synthesis of Palladium Nanocrystals in Aqueous Solution with Systematic Shape Evolution. *Langmuir* **2015**, *31*, 6538–6545.
- (39) Heggen, M.; Oezaslan, M.; Houben, L.; Strasser, P. Formation and Analysis of Core–Shell Fine Structures in Pt Bimetallic Nanoparticle Fuel Cell Electrocatalysts. *J. Phys. Chem. C* **2012**, *116*, 19073–19083.
- (40) Niu, W.; Zhang, L.; Xu, G. Shape-Controlled Synthesis of Single-Crystalline Palladium Nanocrystals. *ACS Nano* **2010**, *4*, 1987–1996.
- (41) Xia, X.; Wang, Y.; Ruditskiy, A.; Xia, Y. 25th Anniversary Article: Galvanic Replacement: A Simple and Versatile Route to Hollow Nanostructures with Tunable and Well-Controlled Properties. *Adv. Mater.* **2013**, *25*, 6313–6333.
- (42) Xia, Y.; Xia, X.; Peng, H.-C. Shape-Controlled Synthesis of Colloidal Metal Nanocrystals: Thermodynamic versus Kinetic Products. *J. Am. Chem. Soc.* **2015**, *137*, 7947–7966.
- (43) Zou, H.; Wang, R.; Dai, J.; Wang, Y.; Wang, X.; Zhang, Z.; Qiu, S. Amphiphilic Hollow Porous Shell Encapsulated Au@Pd Bimetal Nanoparticles for Aerobic Oxidation of Alcohols in Water. *Chem. Commun.* **2015**, *51*, 14601–14604.
- (44) Ding, Y.; Fan, F.; Tian, Z.; Wang, Z. L. Atomic Structure of Au–Pd Bimetallic Alloyed Nanoparticles. *J. Am. Chem. Soc.* **2010**, *132*, 12480–12486.
- (45) Liu, H. B.; Pal, U.; Perez, R.; Ascencio, J. A. Structural Transformation of Au–Pd Bimetallic Nanoclusters on Thermal Heating and Cooling: A Dynamic Analysis. *J. Phys. Chem. B* **2006**, *110*, 5191–5195.
- (46) Metin, O.; Sun, X.; Sun, S. Monodisperse Gold–Palladium Alloy Nanoparticles and Their Composition-Controlled Catalysis in Formic Acid Dehydrogenation under Mild Conditions. *Nanoscale* **2013**, *5*, 910–912.
- (47) Mie, G. Beiträge zur Optik trüber Medien, speziell kolloidaler Metallösungen. *Ann. Phys.* **1908**, *330*, 377–445.
- (48) Jain, P. K.; Lee, K. S.; El-Sayed, I. H.; El-Sayed, M. A. Calculated Absorption and Scattering Properties of Gold Nanoparticles of Different Size, Shape, and Composition: Applications in Biological Imaging and Biomedicine. *J. Phys. Chem. B* **2006**, *110*, 7238–7248.